

# Implicit Grid Convolution for Multi-Scale Image Super-Resolution

Dongheon Lee      Seokju Yun      Youngmin Ro\*

University of Seoul

Code: <https://github.com/dslisleedh/IGConv>

{dslisleedh, wsz871, youngmin.ro}@uos.ac.kr

## Abstract

For Image Super-Resolution (SR), it is common to train and evaluate scale-specific models composed of an encoder and upsampler for each targeted scale. Consequently, many SR studies encounter substantial training times and complex deployment requirements. In this paper, we address this limitation by training and evaluating multiple scales simultaneously. Notably, we observe that encoder features are similar across scales and that the Sub-Pixel Convolution (SPConv), widely-used scale-specific upsampler, exhibits strong inter-scale correlations in its functionality. Building on these insights, we propose a multi-scale framework that employs a single encoder in conjunction with Implicit Grid Convolution (IGConv), our novel upsampler, which unifies SPConv across all scales within a single module. Extensive experiments demonstrate that our framework achieves comparable performance to existing fixed-scale methods while reducing the training budget and stored parameters three-fold and maintaining the same latency. Additionally, we propose IGConv<sup>+</sup> to improve performance further by addressing spectral bias and allowing input-dependent upsampling and ensembled prediction. As a result, ATD-IGConv<sup>+</sup> achieves a notable 0.21dB improvement in PSNR on Urban100×4, while also reducing the training budget, stored parameters, and inference cost compared to the existing ATD.

## 1. Introduction

Image Super-Resolution (SR) aims to restore a High-Resolution Image ( $I^{HR}$ ) from a Low-Resolution Image ( $I^{LR}$ ) input, which is one of the most fundamental challenges in computer vision and graphics. Over a decade ago, SRCNN [9] successfully introduced neural networks to SR, leading to significant performance improvements. Following SRCNN, many previous studies have focused on improving performance by proposing new core operators or larger models, leading to massive models like HAT-Large [5] that leverage up to 41 million parameters.

\*Corresponding Author

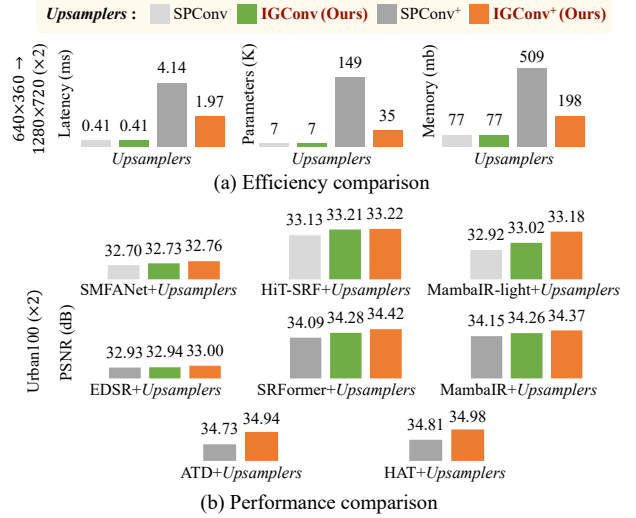


Figure 1. Efficiency and performance comparison on existing upsampler (SPConv and SPConv<sup>+</sup>) with our proposals (IGConv and IGConv<sup>+</sup>) on various metrics and models. Efficiency metrics are measured by reconstructing an HD (1280×720) image on an A6000 GPU after instantiating our proposals on a ×2 scale.

In general, classic SR methods train and evaluate a single scale-specific model for each target scale [9, 21]. Since SR tasks typically consider three scales (×2, ×3, and ×4), the training budget and stored parameters are significantly increased by a factor of three. As the size of models and datasets increases and training strategies become more complex, the time required for training has grown substantially. For instance, training a large model with 20 million parameters [12] for ×2 scale using four A6000 GPUs takes approximately 241 hours. This issue is expected to become more pronounced in the future. Also, from a deployment perspective, storing and loading SR models for every target size is a significant restriction when computing resource-constrained scenarios like real-world applications.

In this paper, we present a novel multi-scale framework, developed through an in-depth investigation, that employs a single encoder and a single upsampler pair. In our preliminary study assessing the similarity between features extracted from different encoders trained at various scales, we

Table 1. Comparisons of various upsamplers employing RDN [43] encoder. The efficiency metrics are measured by upsampling a  $256 \times 256$  image for scale  $\times 4$  using an A6000 GPU.

Upsampler @RDN [43]	Type	Latency (ms)	Memory (mb)	Urban100 (PSNR $\uparrow$ )		
				$\times 2$	$\times 3$	$\times 4$
SPConv <sup>+</sup>	Fixed	5.5	529.1	32.89	28.80	26.61
LM-LTE [13]	Arb.	95.7	1442.4	33.03	28.96	26.80
IGConv <sup>+</sup> (Ours)	Multi.	3.9	193.5	33.17	29.11	26.96

observe that features from the later stages of these encoders exhibit significant similarity. This characteristic is consistently present across models utilizing various core operators such as convolution [44], self-attention [41], and state-space models (SSM) [12]. These findings provide valuable insight into the potential for training multiple scales with a single encoder. Building upon this, utilizing upsamplers capable of inferring any scale, as proposed in the Arbitrary-Scale Super-Resolution (ASSR) domain, appears to be straightforward. However, as shown in Table 1, the upsamplers from ASSR require excessive computational cost for inefficient architecture to predict non-integer scales. Therefore, we focus on the structural mechanism of the widely used scale-specific upsampler, Sub-Pixel Convolution (SPConv), and observe that the goal of upsampling filters at different scales is highly analogous. For example, as shown in Figure 4, the filtered sub-pixels exhibit significant correlations across scales within the 2D space. Building on this insight, we propose Implicit Grid Convolution (IGConv), which unifies SPConv at all scales, enabling multi-scale predictions while maintaining the same latency.

Moreover, we propose IGConv<sup>+</sup>, which boosts performance further by addressing spectral bias and enabling input-dependent upsampling and ensembled prediction. We leverage frequency loss to mitigate spectral bias and introduce Implicit Grid Sampling (IGSample) designed to handle both spectral bias and input-dependent upsampling. Additionally, we introduce a feature-level geometric reparameterization (FGRep), which enables ensemble prediction with a single forward pass. As a result, applying IGConv to existing scales-specific methods achieves comparable performance while reducing the training budget and stored parameters by one-third and maintaining the same latency. Furthermore, applying IGConv<sup>+</sup> to methods such as EDSR [22], SRFormer [45], and MambaIR [12] improves PSNR by 0.16 dB, 0.25 dB, and 0.12 dB, respectively, on Urban100 $\times 4$  still reducing substantial training overheads. Moreover, even for large-size models adopting ImageNet pre-training strategy [5], our methods impressively reduce training time by up to 552 hours.

Our contributions are summarized as follows:

- We highlight the inefficiency of the classic fixed-scale approaches and address it by proposing the multi-scale frame employing a single encoder and IGConv.
- Furthermore, we propose IGConv<sup>+</sup>, which improves performance by employing frequency loss and introducing IGSample, and FGRep.

- As a result, SRFormer-IGConv<sup>+</sup> achieves remarkable 0.33 dB improvement on Urban100 $\times 2$  compared to the existing SRFormer, as shown in Figure 1.

## 2. Related Work

**Classic Image Super-Resolution** From early on to the present, CNN-based methods, which primarily utilize convolution operations suited for image processing due to their local bias and translation invariance, have been foundational in SR tasks [9, 22, 29, 42, 44]. Recently, transformers [10, 35] have garnered significant attention in SR tasks due to their ability to handle long-range dependencies and their advantage of leveraging dynamic weights. Methods that compute self-attention within a window patch [21] or in a transposed manner (channel-wise) [37] to reduce the number of pixels processed at once for the quadratic complexity of self-attention have demonstrated superior performance with reduced computational complexity and parameters. Building on the success of window/transposed self-attention, studies have continued to report improvements in various aspects: widening receptive fields [5, 28, 39, 45], spectral bias [20], quadratic complexity [7, 41], and memory inefficiency [24, 40]. In contrast, MambaIR [12] successfully introduced SSM [11], a promising alternative to self-attention, to low-level vision tasks including SR by enhancing their local mixing ability and intermediate feature representation.

Almost all listed studies adopt the fixed-scale approach employing SPConv for upsampling. Instead, we propose a multi-scale framework employing a single encoder and IGConv to train multiple scales simultaneously.

**Multi/Arbitrary-Scale Super-Resolution** Dissimilar from the classic image SR methods, there have been experimental studies that can predict more than a single scale. For example, LapSRN [18] proposed progressively upsampling architecture to predict  $\times 8$  scale reliably, MDSR [22] shared a feature extractor across three scales with scale-specific heads and tails. MetaSR [14] proposed the meta-upscaling module that performs convolution with pixel-wise dynamic filters for ASSR. Recently, research in the ASSR field has gained significant attention by adopting Implicit Neural Representation (INR) from the graphics domain [27]. LIIF [6] predicts RGB employing MLPs with 2D relative position, nearby four feature vectors, and cell decoding. Subsequent studies have focused on improving aspects such as the spectral bias [19], local ensemble [3, 4], scale-equivalence [36], and efficiency [13, 30, 34].

While our approach shares similarities with ASSR methods by training multiple scales simultaneously using INR-based methods, it differs in that we do not specifically target arbitrary scales. Furthermore, we demonstrate that our method is superior to existing multi-scale SR methods in Appendix 7.

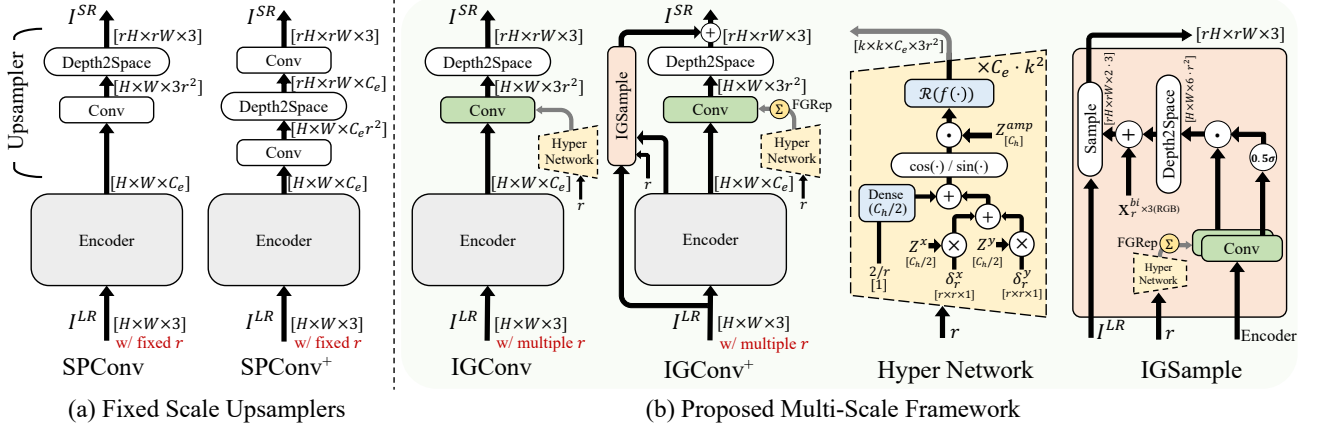


Figure 2. The structure of SR models. (a) illustrates the classic fixed-scale SR methods employing SPCnv and SPCnv<sup>+</sup>, while (b) illustrates our multi-scale frameworks employing IGConv, and IGConv<sup>+</sup>. Our proposed methods comprise the hyper-network to generate convolution filters based on scale and employ the IGSample as a sub-module for efficient input-dependent upsampling. FGRep is employed to improve performance by performing ensemble prediction with a single forward pass.

### 3. Proposed Methods

This section describes the structure of classical SR models and presents the preliminary analyses that lead us to train multiple integer scales simultaneously with a single model. Based on the analyses, we use a single encoder for all scales and introduce our novel upsampler, IGConv, which efficiently predicts multiple integer scales. Following that, we describe the methods added to IGConv<sup>+</sup> – frequency loss, IGSample, and FGRep – to enhance performance further.

#### 3.1. Structure of SR Models

As shown in Figure 2, the structure of classical SR models can be presented as:

$$\begin{aligned} M &= \mathcal{E}(I^{LR}), \\ I^{SR} &= \mathcal{U}(M, r), \end{aligned} \quad (1)$$

where  $\mathcal{E}$  denotes the encoder that extracts deep feature representation  $M \in \mathbb{R}^{H \times W \times C_e}$  with the same resolution as the input  $I^{LR} \in \mathbb{R}^{H \times W \times 3}$ , and  $\mathcal{U}$  represents the upsampler that produces high-resolution output  $I^{SR} \in \mathbb{R}^{rH \times rW \times 3}$  according to a scale factor  $r$ .

#### 3.2. Preliminary Analysis

Numerous SR methods [5, 12, 22, 39, 41, 44, 45] train and evaluate scale-specific models on each targeted scale, even though their encoders share the exact same structure. The scale-specific encoders require their own training budget and storage space, significantly increasing computing resources. This raises the question of whether the benefits of scale-specific encoders justify the significant additional computational resources required. To verify this question, we compare the features extracted by encoders at different scales by analyzing their CKA similarity [17] across various core operators and model sizes [12, 41, 44]. □ As shown in

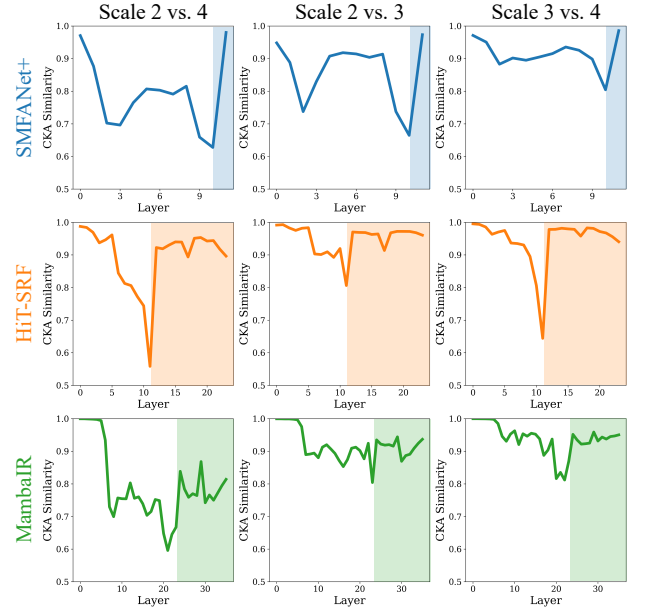


Figure 3. Visualization of CKA similarity [17] between feature maps at scale  $\times 2$ ,  $\times 3$ , and  $\times 4$  varying layers of SMFANet+ [44], HiT-SRF [41], and MambaIR [12]. CKA similarity demonstrates that feature maps at different scales become increasingly similar as they approach the later layer.

Figure 3, surprisingly, the CKA similarity of feature maps between different scales exceeds 0.9 on average, indicating that encoders at different scales tend to extract similar features. This high similarity suggests that scale-specific encoders may not be necessary, given the substantial overlap in the features they capture. Consequently, we leverage only a single encoder to train multiple integer scales.

For the next step, we investigate the mechanism of the SPCnv, a commonly used and efficient scale-specific up-

sampler. Upon detailed visualization of SPConv, we observe that, although SPConv at different scales uses varying numbers of convolution filters, it shares a common goal. Specifically, it divides each LR pixel (denoted as a *grid* and illustrated by the black bolded lines in Figure 4) into  $r^2$  sub-pixels. Furthermore, these  $r^2$  sub-pixels exhibit strong inter-scale correlation in 2D space due to the subsequent depth-to-space (*DS*) operation. This observation suggests that SPConvs at different scales fundamentally operate in the same way. Consequently, SPConvs across all scales can be unified into a single module based on this similarity.

### 3.3. Implicit Grid Convolution

We propose IGConv, which integrates SPConv across all scales by parameterizing convolution filters that predict sub-pixels with inter-scale correlations employing hyper-network. Specifically, the inter-scale correlations denote the size and relative position of sub-pixels that vary with  $r$ . IGConv consists of three main components: the hyper-network, convolution operation, and upsampling operation. These can be represented as follows:

$$\begin{aligned} K &= \mathcal{H}(r), \\ M' &= M * K, \\ I^{SR} &= \mathcal{DS}(M', r), \end{aligned} \quad (2)$$

where  $\mathcal{H}$  represents the hyper-network that generates the convolution filter  $K \in \mathbb{R}^{k \times k \times C_e \times 3 \cdot r^2}$  according to  $r$ , and  $M' \in \mathbb{R}^{H \times W \times 3 \cdot r^2}$  refers to the feature map obtained by convolving  $M$  with  $K$ .  $M'$  is then passed through the upsampling operation  $\mathcal{DS}(\cdot) : \mathbb{R}^{H \times W \times 3 \cdot r^2} \mapsto \mathbb{R}^{rH \times rW \times 3}$ , resulting in  $I^{SR}$ .

Since  $\mathcal{H}$  only depends on  $r$ , it can be pre-computed to targeted scales and excluded during the inference phase, making the instantiated IGConv functionally identical to SPConv. Furthermore, because IGConv does not add any modules to the utilized encoder, the model with instantiated IGConv maintains the same inference cost and parameters as the scale-specific model employing SPConv. Even when training, additional computations, and parameters brought by IGConv are negligible compared to those brought by scale-specific encoders and upsamplers.

**Hyper-Network** The hyper-network uses INR-based methods to generate  $K$  depending on the inter-scale correlations formulated as:

$$\begin{aligned} F_r &= h(r), \\ K &= \mathcal{R}(f(F_r)), \end{aligned} \quad (3)$$

where  $h$  represents the coefficient estimator that generates Fourier coefficients  $F_r \in \mathbb{R}^{C_e \cdot k^2 \times r \times r \times C_h}$  according to the  $r$ , and  $f(\cdot) \in \mathbb{R}^{C_e \cdot k^2 \times r \times r \times C_h} \mapsto \mathbb{R}^{C_e \cdot k^2 \times r \times r \times 3}$  is parameterized MLPs with ReLU activations that predict intermediate representations from  $F_r$ . Lastly,  $\mathcal{R}(\cdot) \in$

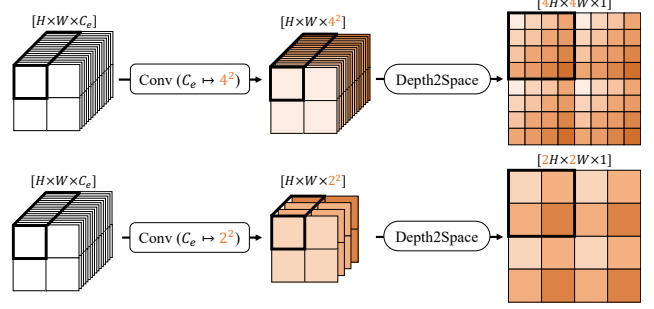


Figure 4. Visualization of SPConv for scales 4 and 2. Although the SPConvs at different scales employ different numbers of filters, the filtered sub-pixels for all scales exhibit significant 2D spatial correlations (illustrated with color gradients) due to the subsequent *DS*. Visualized convolution filters trained to capture inter-scale correlations are shown in Figure 5.

$\mathbb{R}^{C_e \cdot k^2 \times r \times r \times 3} \mapsto \mathbb{R}^{k \times k \times C_e \times 3r^2}$  denotes the reshape operation that converts the predicted intermediate representations into  $K$ , convolution filters for scale-specific modulation. Specifically,  $F_r$  is inferred by the following process:

$$\begin{aligned} C_r &= \langle \delta_r^x, Z^x \rangle + \langle \delta_r^y, Z^y \rangle, s_r = h^s(2/r), \\ F_r &= Z^{amp} \odot \begin{bmatrix} \cos(\pi(C_r + s_r)) \\ \sin(\pi(C_r + s_r)) \end{bmatrix}, \end{aligned} \quad (4)$$

where  $Z^{amp} \in \mathbb{R}^{C_h}$  denotes the scale-invariant latent code,  $C_r \in \mathbb{R}^{C_e \cdot k^2 \times r \times r \times C_h}$  refers to the coordinate matrix representing the relative coordinates according to the  $r$ , and  $s_r$  represents the size according to the  $r$ .  $F_r$  is created by element-wisely multiplying the scale-variant Fourier matrix, formed by  $C_r$  and  $s_r$ , with  $Z^{amp}$ .  $C_r$  is generated by matrix multiplying the uniformly sampled 2D regular coordinates  $\delta_r^x, \delta_r^y \in [-1, 1]^{1 \times r \times r \times 1}$  with the scale-invariant latent codes  $Z^x, Z^y \in \mathbb{R}^{C_e \cdot k^2 \times 1 \times 1 \times C_h/2}$  respectively, and then summing the results.  $s_r$  is generated by feeding the reciprocal of the  $r$ , proportional to the size to be predicted sub-pixels, into a single linear layer ( $h^s$ ).

In summary, the convolution filters are estimated from the size and regular coordinates evenly distributed by  $r \times r$  in 2D space. These attributes correspond to the size and coordinates of  $r^2$  filtered sub-pixels in each grid after *DS*. Since filtered sub-pixels of SPConv at any scale can be represented in the same way,  $\mathcal{H}$  can effectively predict convolutional filters at any integer scale for upsampling.

### 3.4. Frequency Loss

Mapping signals employing MLPs induces spectral bias [19]. Therefore, in addition to the commonly used pixel-wise L1 loss, we leverage frequency loss [31, 33] to make the model focus on high-frequency detail, as follows:

$$\mathcal{L} = \|I^{HR} - I^{SR}\|_1 + \lambda \|\mathcal{F}(I^{HR}) - \mathcal{F}(I^{SR})\|_1, \quad (5)$$



Table 2. Comparisons of fixed-scale upsamplers (SPConv, SPConv<sup>+</sup>) and our proposed multi-scale upsamplers (IGConv, IGConv<sup>+</sup>) on various encoders trained on the DIV2K dataset. Results from SPConv( $\times r$ ) and SPConv<sup>+</sup>( $\times r$ ) are measured by each scale-specific model, while results from IGConv and IGConv<sup>+</sup> are measured by a **single model**. The only best result is bolded.

Dataset	Scale	Encoder (Operator)	Upsampler	Set5	Set14	B100	Urban100	Manga109
DIV2K	2	EDSR [22] (CNN)	SPConv <sup>+</sup> ( $\times 2$ )	38.11/0.9602	33.92/0.9195	32.32/0.9013	32.93/0.9351	39.10/0.9773
			IGConv	38.21/0.9612	33.96/0.9209	32.34/0.9016	32.94/0.9359	39.13/0.9780
			<b>IGConv<sup>+</sup></b>	<b>38.24/0.9614</b>	33.96/0.9209	<b>32.34/0.9018</b>	<b>33.00/0.9360</b>	<b>39.25/0.9783</b>
		HiT-SRF [41] (Transformer)	SPConv( $\times 2$ )	38.26/0.9615	34.01/0.9214	32.37/0.9023	33.13/0.9372	39.47/0.9787
			IGConv	38.16/0.9604	<b>34.02/0.9214</b>	32.35/0.9020	33.21/0.9377	39.34/0.9781
			<b>IGConv<sup>+</sup></b>	<b>38.30/0.9615</b>	33.97/0.9210	<b>32.38/0.9023</b>	<b>33.22/0.9377</b>	39.47/0.9786
	3	EDSR [22] (CNN)	SPConv( $\times 2$ )	38.16/0.9610	34.00/0.9212	32.34/0.9017	32.92/0.9356	39.31/0.9779
			IGConv	38.20/0.9611	34.02/0.9214	32.34/0.9014	33.02/0.9365	39.28/0.9782
			<b>IGConv<sup>+</sup></b>	<b>38.20/0.9613</b>	<b>34.11/0.9221</b>	<b>32.36/0.9019</b>	<b>33.18/0.9372</b>	<b>39.44/0.9786</b>
		HiT-SRF [41] (Transformer)	SPConv( $\times 3$ )	34.65/0.9280	30.52/0.8462	29.25/0.8093	28.80/0.8653	34.17/0.9476
			IGConv	34.70/0.9294	30.56/0.8469	29.28/0.8097	28.90/0.8671	34.31/0.9491
			<b>IGConv<sup>+</sup></b>	<b>34.74/0.9298</b>	<b>30.65/0.8481</b>	<b>29.30/0.8103</b>	<b>28.95/0.8675</b>	<b>34.47/0.9496</b>
	4	EDSR [22] (CNN)	SPConv( $\times 3$ )	34.75/0.9300	30.61/0.8475	29.29/0.8106	28.99/0.8687	34.53/0.9502
			IGConv	34.69/0.9292	30.60/0.8476	29.26/0.8098	29.02/0.8694	34.46/0.9499
			<b>IGConv<sup>+</sup></b>	<b>34.78/0.9302</b>	<b>30.69/0.8488</b>	<b>29.32/0.8111</b>	<b>29.06/0.8693</b>	<b>34.67/0.9506</b>
		MambaIR-lt [12] (SSM)	SPConv( $\times 3$ )	34.72/0.9296	30.63/0.8475	29.29/0.8099	29.00/0.8689	34.39/0.9495
			IGConv	34.70/0.9294	30.59/0.8474	29.27/0.8094	28.91/0.8672	34.37/0.9492
			<b>IGConv<sup>+</sup></b>	<b>34.74/0.9298</b>	<b>30.68/0.8487</b>	<b>29.30/0.8105</b>	<b>29.04/0.8687</b>	<b>34.62/0.9502</b>
	5	EDSR [22] (CNN)	SPConv <sup>+</sup> ( $\times 4$ )	32.46/0.8968	28.80/0.7876	27.71/0.7420	26.64/0.8033	31.02/0.9148
			IGConv	32.57/0.8990	28.84/0.7880	27.76/0.7426	26.75/0.8060	31.29/0.9178
			<b>IGConv<sup>+</sup></b>	<b>32.59/0.8996</b>	<b>28.91/0.7890</b>	<b>27.79/0.7433</b>	<b>26.82/0.8064</b>	<b>31.43/0.9182</b>
		HiT-SRF [41] (Transformer)	SPConv( $\times 4$ )	32.55/0.8999	28.87/0.7880	27.75/0.7432	26.80/0.8069	31.26/0.9171
			IGConv	32.53/0.8988	28.90/0.7887	27.71/0.7422	26.88/0.8085	31.31/0.9184
			<b>IGConv<sup>+</sup></b>	<b>32.60/0.9001</b>	<b>28.95/0.7892</b>	<b>27.80/0.7440</b>	<b>26.91/0.8083</b>	<b>31.57/0.9198</b>
	6	EDSR [22] (CNN)	SPConv( $\times 4$ )	32.51/0.8993	28.85/0.7876	27.75/0.7423	26.75/0.8051	31.26/0.9175
			IGConv	32.50/0.8992	28.86/0.7879	27.75/0.7422	26.72/0.8045	31.29/0.9175
			<b>IGConv<sup>+</sup></b>	<b>32.62/0.8997</b>	<b>28.93/0.7893</b>	<b>27.80/0.7437</b>	<b>26.87/0.8068</b>	<b>31.51/0.9185</b>
		HiT-SRF [41] (Transformer)	SPConv( $\times 4$ )	32.55/0.8999	28.87/0.7880	27.75/0.7432	26.80/0.8069	31.26/0.9171
			IGConv	32.53/0.8988	28.90/0.7887	27.71/0.7422	26.88/0.8085	31.31/0.9184
			<b>IGConv<sup>+</sup></b>	<b>32.60/0.9001</b>	<b>28.95/0.7892</b>	<b>27.80/0.7440</b>	<b>26.91/0.8083</b>	<b>31.57/0.9198</b>

where  $\mathcal{F}$  denotes the Fast Fourier transform, and  $\lambda$  is a weight parameter set to be 0.05 empirically.

### 3.5. Implicit Grid Sampling

SPConv’s performance is limited since it upscales the  $M$  without utilizing the rich representation from it. For this reason, many SR studies focusing on performance improvements [5, 12, 22, 39, 45] employ SPConv<sup>+</sup>, which leverages extra convolution after  $\mathcal{DS}$  (see Figure 2 (a)). However, the extra convolution in high-resolution (HR) space brings significant computational overhead, increasing SPConv<sup>+</sup>’s latency nearly 10 $\times$  over SPConv, as shown in Table 5. To address this limitation, we propose an IGSample inspired by previous research aimed at upsampling feature maps [23], as formulated below:

$$\begin{aligned}
K^o, K^s &= \mathcal{H}_S(r), \\
\delta^{xy} &= (M * K^o) \odot 0.5\sigma(M * K^s), \\
\mathbf{x}_r &= \mathbf{x}_r^{bi} + \mathcal{DS}(\delta^{xy}, r), \\
I^\uparrow &= \mathcal{S}(I^{LR}, \mathbf{x}_r),
\end{aligned} \tag{6}$$

where  $\mathcal{H}_S$  denotes hyper-network to predict convolution filters  $K^o, K^s \in \mathbb{R}^{k \times k \times C_e \times 6 \times r^2}$  depending on  $r$  similar with the  $\mathcal{H}$  in IGConv.  $K^o$  and  $K^s$  are convolution filters to predict the 2D direction and constraint scope for bilinear upsampling ( $\mathcal{S}$ ) on each RGB space. After applying a

sigmoid ( $\sigma$ ) and multiplying 0.5 to the predicted scope, it is multiplied element-wise with the direction to generate calibrating offset  $\delta^{xy} \in \mathbb{R}^{H \times W \times 6 \times r^2}$ . Subsequently,  $\delta^{xy}$  is upsampled through  $\mathcal{DS}$ , then added to  $\mathbf{x}_r^{bi} \in \mathbb{R}^{rH \times rW \times 6}$ , which indicates the coordinates for  $\mathcal{S}$  that is repeated three times channel-wise to represent each RGB space. Finally, the upsampled image  $I^\uparrow$  is created by performing  $\mathcal{S}$  from  $I_{LR}$  in each RGB space based on  $\mathbf{x}_r$  and then added to  $I^{SR}$ .

As a result, our IGSample upsamples  $I^{LR}$  input-dependently by adjusting the coordinates for  $\mathcal{S}$  leveraging the rich information from  $M$ . IGSample also reduces spectral bias by adding low-frequency biased upsampled image [19] to  $I^{SR}$ .

### 3.6. Feature-level Geometric Re-param.

We propose FGRep inspired by input-level geometric ensemble [22] and feature-level local ensemble [6] to improve performance by enabling ensemble prediction, defined as follows:

$$M' = \frac{1}{8} \sum_{i=1}^8 \mathcal{A}_i^{-1}(\mathcal{A}_i(M) * K), \tag{7}$$

where  $\mathcal{A}$  refers to augmentation functions that consist of 8 transformations, including flip, rotation, and identity. Each  $\mathcal{A}$  applies on  $M$  to create an augmented version of  $M$ , followed by convolution with  $K$ . Then, inverse augmentation  $\mathcal{A}^{-1}$  is applied to each filtered output to revert them to their

Table 3. Comparisons of fixed-scale upsamplers (SPConv, SPConv<sup>+</sup>) and our proposed multi-scale upsamplers (IGConv, IGConv<sup>+</sup>) on various encoders trained on the DF2K dataset. Results from SPConv( $\times r$ ) and SPConv<sup>+</sup>( $\times r$ ) are measured by each scale-specific model, while results from IGConv and IGConv<sup>+</sup> are measured by a **single model**. The only best result is bolded.

Dataset	Scale	Encoder (Operator)	Upsampler	Set5	Set14	B100	Urban100	Manga109
DF2K	2	SMFANet+ [44] (CNN)	SPConv ( $\times 2$ )	<b>38.19</b> /0.9611	33.92/0.9207	32.32/ <b>0.9015</b>	32.70/0.9331	<b>39.46</b> /0.9787
			IGConv	38.16/0.9610	<b>33.96</b> /0.9213	32.32/0.9014	32.73/0.9332	39.38/0.9785
			<b>IGConv<sup>+</sup></b>	38.14/0.9611	33.92/0.9208	32.32/0.9014	<b>32.76</b> /0.9334	39.40/0.9786
		SRFormer [45] (Transformer)	SPConv <sup>+</sup> ( $\times 2$ )	38.51/ <b>0.9627</b>	34.44/0.9253	32.57/0.9046	34.09/0.9449	<b>40.07</b> /0.9802
			IGConv	38.44/0.9625	34.64/0.9267	32.56/0.9048	34.28/0.9462	39.88/0.9798
			<b>IGConv<sup>+</sup></b>	<b>38.53</b> /0.9626	<b>34.72</b> /0.9268	<b>32.60</b> /0.9052	<b>34.42</b> /0.9468	40.03/0.9797
		MambaIR [12] (SSM)	SPConv <sup>+</sup> ( $\times 2$ )	<b>38.57</b> /0.9627	34.67/0.9261	32.58/0.9048	34.15/0.9446	<b>40.28</b> /0.9806
			IGConv	38.48/0.9624	34.68/0.9264	32.58/0.9047	34.26/0.9453	40.14/0.9803
			<b>IGConv<sup>+</sup></b>	38.55/0.9625	<b>34.81</b> /0.9270	<b>32.62</b> /0.9052	<b>34.37</b> /0.9461	40.19/0.9802
	3	SMFANet+ [44] (CNN)	SPConv( $\times 3$ )	<b>34.66</b> /0.9292	30.57/0.8461	29.25/0.8090	<b>28.67</b> /0.8611	34.45/0.9490
			IGConv	34.62/0.9290	30.56/0.8461	29.25/0.8090	28.64/0.8606	34.45/0.9490
			<b>IGConv<sup>+</sup></b>	34.58/0.9287	<b>30.58</b> /0.8464	29.24/0.8089	28.66/0.8610	34.45/0.9490
		SRFormer [45] (Transformer)	SPConv <sup>+</sup> ( $\times 3$ )	35.02/0.9323	30.94/0.8540	29.48/0.8156	30.04/0.8865	35.26/0.9543
			IGConv	34.96/0.9323	30.95/0.8543	29.47/0.8157	30.11/0.8876	35.16/0.9543
			<b>IGConv<sup>+</sup></b>	<b>35.08</b> /0.9329	<b>31.06</b> /0.8551	<b>29.52</b> /0.8166	<b>30.25</b> /0.8888	<b>35.45</b> /0.9550
		MambaIR [12] (SSM)	SPConv <sup>+</sup> ( $\times 3$ )	35.08/0.9323	30.99/0.8536	29.51/0.8157	29.93/0.8841	35.43/0.9546
			IGConv	35.04/0.9320	31.01/0.8535	29.50/0.8154	29.95/0.8844	35.44/0.9545
			<b>IGConv<sup>+</sup></b>	<b>35.10</b> /0.9325	<b>31.14</b> /0.8550	<b>29.55</b> /0.8164	<b>30.11</b> /0.8864	<b>35.55</b> /0.9549
	4	SMFANet+ [44] (CNN)	SPConv( $\times 4$ )	32.51/0.8985	<b>28.87</b> /0.7872	27.74/0.7412	<b>26.56</b> /0.7976	31.29/ <b>0.9163</b>
			IGConv	32.47/0.8982	28.84/0.7866	27.74/0.7413	26.54/0.7969	31.28/0.9158
			<b>IGConv<sup>+</sup></b>	<b>32.52</b> /0.8988	28.83/0.7867	27.74/0.7413	26.55/0.7974	31.29/0.9161
		SRFormer [45] (Transformer)	SPConv <sup>+</sup> ( $\times 4$ )	32.93/0.9041	29.08/0.7953	27.94/0.7502	27.68/0.8311	32.21/0.9271
			IGConv	32.87/0.9046	29.08/0.7952	27.91/0.7499	27.79/0.8333	32.14/0.9274
			<b>IGConv<sup>+</sup></b>	<b>33.04</b> /0.9047	<b>29.22</b> /0.7971	<b>27.99</b> /0.7509	<b>27.93</b> /0.8350	<b>32.45</b> /0.9288
		MambaIR [12] (SSM)	SPConv <sup>+</sup> ( $\times 4$ )	33.03/0.9046	29.20/0.7961	27.98/0.7503	27.68/0.8287	32.32/0.9272
			IGConv	32.98/0.9041	29.17/0.7955	27.97/0.7498	27.68/0.8288	32.36/0.9271
			<b>IGConv<sup>+</sup></b>	<b>33.05</b> /0.9045	<b>29.25</b> /0.7969	<b>28.02</b> /0.7512	<b>27.80</b> /0.8314	<b>32.52</b> /0.9280

original state, and all filtered outputs are averaged to produce  $M'$ . The  $\mathcal{H}$ , and  $\mathcal{DS}$  in IGConv are omitted.

This is similar to the local ensemble as it performs the ensemble on the final feature  $M$  and is also similar to the geometric ensemble in how augmentations are applied. Interestingly, performing convolution on augmented feature maps with a single kernel followed by inverse augmentation is equivalent to applying convolution to a single feature map with augmented kernels, leading to the redefinition of Equation 7 as follows:

$$M' = \frac{1}{8} \sum_{i=1}^8 M * \mathcal{A}_i(K). \quad (8)$$

Furthermore, performing convolution on a single feature map with multiple kernels and then summing up results can be converted to performing convolution on a single feature map with a single kernel via structural re-parameterization [8]. Equation 8 is redefined by structural re-parameterization as:

$$M' = M * \bar{K}, \quad (9)$$

where  $\bar{K} = \frac{1}{8} \sum_{i=1}^8 \mathcal{A}_i(K).$

Consequently, FGRep allows the upsampler to produce en-

sembled predictions with only a single forward pass during the inference phase. We apply FGRep to every kernel predicted by the hyper-networks ( $K, K^o, K^s$ ).

## 4. Experiments

### 4.1. Training Strategy

This section describes the training strategy to train multiple integer scales simultaneously. We randomly sample a scale from  $r \in \{2, 3, 4\}$  for each batch, commonly used scales in SR tasks. After that, we crop a patch ( $I_{HR}$ ) from a high-quality image ( $I_{GT}$ ) to the size of the training patch multiplied by the sampled scale.  $I_{HR}$  is then bicubic down-sampled by the randomly sampled scale to create  $I_{LR}$ , and the model is trained to reconstruct  $I_{HR}$  from  $I_{LR}$ . Since IGConv can only upsample a single scale per batch, we optimize the model by utilizing generalized gradients averaged across multiple sub-batches. This approach can be implemented by gradient accumulation or distributed learning, and we use distributed learning with 4 GPUs. *In all cases, we train multi-scale simultaneously employing IGConv or IGConv<sup>+</sup> with only the training budget that existing methods employing SPConv or SPConv<sup>+</sup> used for a single scale, thereby reducing training budget (training time or GPU demands) by one-third.*

Table 4. Comparisons of SPConv<sup>+</sup> and IGConv<sup>+</sup> on the methods adopting the pre-training strategy. Results from SPConv<sup>+</sup>( $\times r$ ) are measured by each scale-specific model, while results from IGConv<sup>+</sup> are measured by **a single model**. The best and the second-best results are bolded and underlined, respectively.

Pre-train	Scale	Encoder	Upsampler	Set5	Set14	B100	Urban100	Manga109
DF2K	$\times 2$	ATD [39]	SPConv <sup>+</sup> ( $\times 2$ )	38.61/0.9629	34.92/0.9275	32.64/0.9054	34.73/0.9476	40.35/0.9810
			<b>IGConv<sup>+</sup></b>	<u>38.68/0.9631</u>	<u>35.00/0.9280</u>	<u>32.69/0.9059</u>	<u>34.94/0.9491</u>	<u>40.29/0.9804</u>
ImageNet		HAT [5]	SPConv <sup>+</sup> ( $\times 2$ )	<b>38.73/0.9637</b>	<b>35.13/0.9282</b>	<b>32.69/0.9060</b>	<b>34.81/0.9489</b>	<b>40.71/0.9819</b>
			<b>IGConv<sup>+</sup></b>	<u>38.68/0.9631</u>	<b>35.16/0.9282</b>	<b>32.71/0.9060</b>	<b>34.98/0.9494</b>	<u>40.39/0.9809</u>
DF2K	$\times 3$	ATD [39]	SPConv <sup>+</sup> ( $\times 3$ )	35.15/0.9331	31.15/0.8556	29.58/0.8175	30.52/0.8924	35.64/0.9558
			<b>IGConv<sup>+</sup></b>	<b>35.17/0.9334</b>	<u>31.22/0.8564</u>	<u>29.61/0.8183</u>	<u>30.76/0.8946</u>	<u>35.84/0.9565</u>
ImageNet		HAT [5]	SPConv <sup>+</sup> ( $\times 3$ )	<b>35.16/0.9335</b>	<b>31.33/0.8576</b>	<u>29.59/0.8177</u>	<u>30.70/0.8949</u>	<u>35.84/0.9567</u>
			<b>IGConv<sup>+</sup></b>	<u>35.13/0.9335</u>	<b>31.46/0.8576</b>	<b>29.62/0.8182</b>	<b>30.78/0.8951</b>	<b>35.95/0.9568</b>
DF2K	$\times 4$	ATD [39]	SPConv <sup>+</sup> ( $\times 4$ )	33.14/0.9061	29.25/0.7976	28.02/0.7524	28.22/0.8414	32.65/0.9308
			<b>IGConv<sup>+</sup></b>	33.13/0.9061	29.36/0.7994	<u>28.07/0.7536</u>	<u>28.43/0.8444</u>	<u>32.92/0.9319</u>
ImageNet		HAT [5]	SPConv <sup>+</sup> ( $\times 4$ )	<b>33.18/0.9073</b>	<u>29.38/0.8001</u>	<u>28.05/0.7534</u>	<u>28.37/0.8447</u>	<u>32.87/0.9319</u>
			<b>IGConv<sup>+</sup></b>	<u>33.17/0.9074</u>	<b>29.48/0.8008</b>	<b>28.08/0.7533</b>	<b>28.45/0.8450</b>	<b>33.09/0.9327</b>

## 4.2. Implemtation Details

In this section, we describe the implementation details of our proposal methods. The  $f$  of  $\mathcal{H}$  and  $\mathcal{H}_S$  are composed of 256 and 128 dimensions, respectively, with four and two hidden layers. Additionally,  $C_h$  for  $\mathcal{H}$  and  $\mathcal{H}_S$  are also set to 256 and 128, respectively. In practice, since all intermediate representations in  $\mathcal{H}$  and  $\mathcal{H}_S$  are suitably structured for convolution, we implement the  $f$  employing  $1 \times 1$  convolutions. In all cases,  $k$  is set to 3. We implement our codes based on Pytorch and BasicSR toolbox.

## 4.3. Quantitative Results

To validate the importance of multi-scale training and the superiority of our proposed methods, we compare IGConv and IGConv<sup>+</sup> with SPConv and SPConv<sup>+</sup> on various encoders (EDSR [22], SMFANet [44], HiT-SRF [41], SRFormer [45], MambaIR [12]) with various core operators (convolution, self-attention, and state-space model), datasets (DIV2K [1] and DF2K [32]), and upsampler’s complexity (SPConv, and SPConv<sup>+</sup>), respectively. For evaluation, we use five commonly used datasets (Set5 [2], Set14 [38], B100 [25], Urban100 [15], and Manga109 [26]), and measure Peak Signal to Noise Ratio (PSNR) and Structural Similarity Index Measure (SSIM) in the y-channel after cropping image’s boundary equivalent to the each  $r$ . The training details are provided in the Appendix 9.

In Table 2, and Table 3, IGConv maintains comparable performance to SPConv and SPConv<sup>+</sup> while reducing training budget and stored parameters by one-third, indicating that scale-specific training is not essential. Moreover, SRFormer-IGConv<sup>+</sup> outperforms SRFormer-SPConv<sup>+</sup> by 0.25dB at Urban100 $\times 4$ , highlighting the superior performance of IGConv<sup>+</sup>. This result demonstrates that the additional methods (frequency loss, IGSample, and FGRep) introduced in IGConv<sup>+</sup> contribute significantly to this per-

Table 5. Comparisons on SPConv, SPConv<sup>+</sup>, IGConv, and IGConv<sup>+</sup> on efficiency measures after instantiating our methods for the targeted scales. Metrics are calculated by reconstructing an HD (1280 $\times$ 720) image employing the encoder with 64 channels at an A6000 GPU.

Upsampler	Latency (ms)			Parameters (K)			Memory (mb)		
	$\times 2$	$\times 3$	$\times 4$	$\times 2$	$\times 3$	$\times 4$	$\times 2$	$\times 3$	$\times 4$
SPConv	0.41	0.23	0.25	6.9	15.6	27.7	77.4	46.1	38.9
IGConv <sub>inst</sub>	0.41	0.23	0.25	6.9	15.6	27.7	77.4	46.1	38.9
SPConv <sup>+</sup>	4.14	3.92	4.90	149.4	334.1	297.2	508.8	475.5	467.2
IGConv <sup>+</sup> <sub>inst</sub>	1.97	1.50	1.47	34.6	77.8	138.2	197.9	166.1	156.0

formance improvement. Ablation studies for the proposed methods can be found in Appendix 11.

We further validate IGConv<sup>+</sup> on the methods larger models adopting pre-training strategies [5, 39]. As detailed in Table 4, IGConv<sup>+</sup> outperforms SPConv<sup>+</sup> on Manga109 $\times 4$  employing ATD and HAT as encoders, improving PSNR by 0.27 dB and 0.22dB, respectively. These results suggest that our multi-scale framework improves performance even on larger models or complex training settings including pre-training and fine-tuning, which aligns with recent research trends.

We also compare our methods with SPConv and SPConv<sup>+</sup> on efficiency metrics. As shown in Table 5, IGConv<sub>inst</sub> exhibits the same computational cost as SPConv while reducing substantial training budget and stored parameters. Notably, IGConv<sub>inst</sub><sup>+</sup> demonstrates less latency, parameters, and memory usage than SPConv<sup>+</sup> since all computations are computed in LR space, highlighting our method’s remarkable efficiency.

Finally, we compare SPConv<sup>+</sup> and IGConv<sup>+</sup> on training efficiency measures. As shown in Table 6, IGConv<sup>+</sup> significantly reduces training time by three-fold since it only leverages the training budget for SPConv<sup>+</sup> to train a single scale. Furthermore, IGConv<sup>+</sup> also reduces the number of

parameters by one-third confirming that additional parameters brought by IGConv<sup>+</sup> are negligible to those brought by scale-specific encoders and upsamplers. Note that additional parameters brought by IGConv<sup>+</sup> can be further reduced by instantiating IGConv<sup>+</sup> at the inference phase. These results demonstrate that our multi-scale framework significantly reduces training overheads, highlighting our proposal’s exceptional training efficiency.

Table 6. Comparisons of SPConv<sup>+</sup> and IGConv<sup>+</sup> on training efficiency metrics. All training efficiency metrics are obtained by training HAT [5] using four A6000 GPUs. PT and FT denote pre-training on the ImageNet dataset and fine-tuning on the DF2K dataset. #Params indicates the number of parameters *measured during training phase* including both encoder and upsampler.

Metrics		SPConv <sup>+</sup>				IGConv <sup>+</sup>
		$\times 2$	$\times 3$	$\times 4$	= Total	
Time (h)	PT	210	210	210	= 630	<b>213</b>
	FT	68	68	68	= 204	<b>69</b>
#Params (M)		21	21	21	= 63	<b>22</b>

#### 4.4. Analysis on Inter-Scale Correlations

To illustrate the impact of  $\mathcal{H}$  that maps inter-scale correlations (the size and coordinates of predicted sub-pixels) to convolutional filters, we visualise the convolutional filter in RDN-IGConv<sup>+</sup> at various scales ( $\times 2$ ,  $\times 3$ ,  $\times 4$ , and  $\times 32$ ). As shown in Figure 5, the convolution filters at all scales change continuously in response to the change of  $r$ , indicating that  $\mathcal{H}$  effectively mapped the inter-scale correlation to the convolution filters.

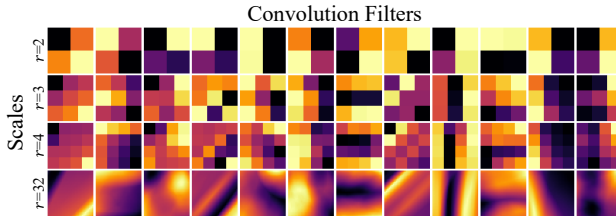


Figure 5. Visualizations of 12 convolution filters in front inferred by  $\mathcal{H}$  of RDN-IGConv<sup>+</sup> for scales  $\times 2$ ,  $\times 3$ ,  $\times 4$ , and  $\times 32$ . More visualizations are provided in the Appendix 12.

#### 4.5. Visual Results

To demonstrate that IGConv and IGConv<sup>+</sup> are also visually superior, we compare our methods visually to SPConv and then to SPConv<sup>+</sup>. As shown in Figure 6, using IGConv and IGConv<sup>+</sup> improves the visual quality and the PSNR. These results demonstrate that our method yields visually pleasing results, emphasizing the potential of learning multi-scale and superior performance of our proposal.

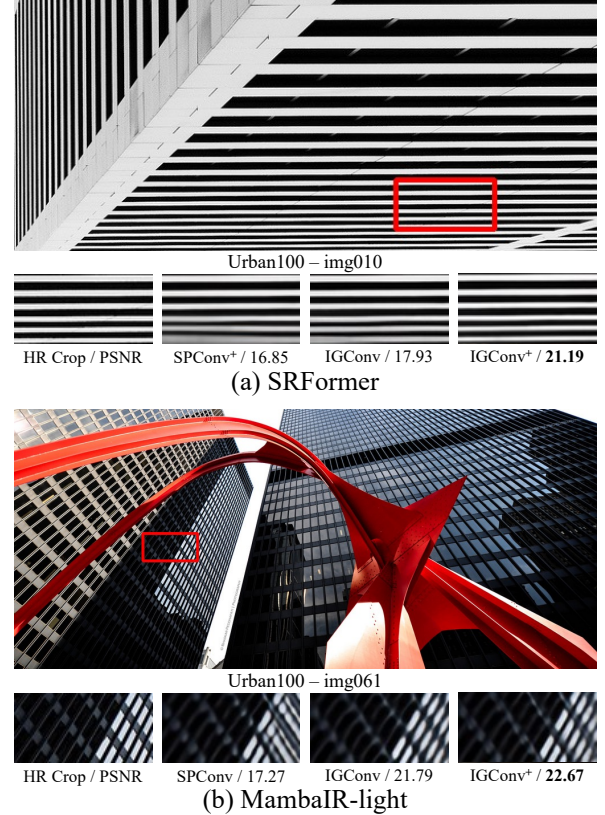


Figure 6. Visual comparisons on SPConv, SPConv<sup>+</sup>, IGConv, and IGConv<sup>+</sup> on Urban100 $\times 4$  dataset. The best results on PSNR are bolded.

## 5. Conclusion

This paper highlighted the inefficiency of the classic fixed-scale SR approach, which employs a scale-specific model for each targeted scale. Based on the observation that encoder features are similar across scales and that SPConv operates in a highly correlated manner, we propose a multi-scale framework that employs a single encoder along with the IGConv. Our multi-scale framework with IGConv significantly reduces both the training budget and parameter storage, achieving consistent performance across various encoders, regardless of its core operator, size, and training dataset. Moreover, we introduced IGConv<sup>+</sup>, which boosts performance by employing frequency loss and introducing IGSample, and FGRep. As a result, our ATD-IGConv<sup>+</sup> achieved a remarkable 0.21 dB improvement in PSNR on Urban100 $\times 4$  also reducing the training budget and stored parameters compared to the existing ATD.

**Discussion:** Multi-scale training with IGConv<sup>+</sup> significantly improved performance, but degree of improvement varies. These variations suggest that a new approach should be considered when proposing architectures suitable for multi-scale training and raise the need for further research.



## References

- [1] Eirikur Agustsson and Radu Timofte. Ntire 2017 challenge on single image super-resolution: Dataset and study. In *CVPRW*, 2017. 7
- [2] Marco Bevilacqua, Aline Roumy, Christine Guillemot, and Marie Line Alberi-Morel. Low-complexity single-image super-resolution based on nonnegative neighbor embedding. 2012. 7
- [3] Jiezhong Cao, Qin Wang, Yongqin Xian, Yawei Li, Bingbing Ni, Zhiming Pi, Kai Zhang, Yulun Zhang, Radu Timofte, and Luc Van Gool. Ciasr: Continuous implicit attention-in-attention network for arbitrary-scale image super-resolution. In *CVPR*, pages 1796–1807, 2023. 2, 3
- [4] Hao-Wei Chen, Yu-Syuan Xu, Min-Fong Hong, Yi-Min Tsai, Hsien-Kai Kuo, and Chun-Yi Lee. Cascaded local implicit transformer for arbitrary-scale super-resolution. In *CVPR*, pages 18257–18267, 2023. 2
- [5] Xiangyu Chen, Xintao Wang, Jiantao Zhou, Yu Qiao, and Chao Dong. Activating more pixels in image super-resolution transformer. In *CVPR*, pages 22367–22377, 2023. 1, 2, 3, 5, 7, 8
- [6] Yinbo Chen, Sifei Liu, and Xiaolong Wang. Learning continuous image representation with local implicit image function. In *CVPR*, pages 8628–8638, 2021. 2, 5, 3, 4
- [7] Zheng Chen, Yulun Zhang, Jinjin Gu, Linghe Kong, and Xiaokang Yang. Recursive generalization transformer for image super-resolution. In *ICLR*, 2024. 2
- [8] Xiaohan Ding, Yuchen Guo, Guiguang Ding, and Jungong Han. Acnet: Strengthening the kernel skeletons for powerful cnn via asymmetric convolution blocks. In *ICCV*, pages 1911–1920, 2019. 6
- [9] Chao Dong, Chen Change Loy, Kaiming He, and Xiaoou Tang. Image super-resolution using deep convolutional networks. *IEEE TPAMI*, 38(2):295–307, 2015. 1, 2
- [10] Alexey Dosovitskiy, Lucas Beyer, Alexander Kolesnikov, Dirk Weissenborn, Xiaohua Zhai, Thomas Unterthiner, Mostafa Dehghani, Matthias Minderer, Georg Heigold, Sylvain Gelly, Jakob Uszkoreit, and Neil Houlsby. An image is worth 16x16 words: Transformers for image recognition at scale. *ICLR*, 2021. 2
- [11] Albert Gu and Tri Dao. Mamba: Linear-time sequence modeling with selective state spaces. *arXiv preprint*, 2023. 2
- [12] Hang Guo, Jinmin Li, Tao Dai, Zhihao Ouyang, Xudong Ren, and Shu-Tao Xia. Mambair: A simple baseline for image restoration with state-space model. In *ECCV*, 2024. 1, 2, 3, 5, 6, 7
- [13] Zongyao He and Zhi Jin. Latent modulated function for computational optimal continuous image representation. In *CVPR*, pages 26026–26035, 2024. 2, 3, 4
- [14] Xuecai Hu, Haoyuan Mu, Xiangyu Zhang, Zilei Wang, Tieniu Tan, and Jian Sun. Meta-sr: A magnification-arbitrary network for super-resolution. In *CVPR*, pages 1575–1584, 2019. 2
- [15] Jia-Bin Huang, Abhishek Singh, and Narendra Ahuja. Single image super-resolution from transformed self-exemplars. In *CVPR*, pages 5197–5206, 2015. 7
- [16] Jiwon Kim, Jung Kwon Lee, and Kyoung Mu Lee. Accurate image super-resolution using very deep convolutional networks. In *CVPR*, pages 1646–1654, 2016. 1
- [17] Simon Kornblith, Mohammad Norouzi, Honglak Lee, and Geoffrey Hinton. Similarity of neural network representations revisited. In *ICML*, pages 3519–3529. PMLR, 2019. 3
- [18] Wei-Sheng Lai, Jia-Bin Huang, Narendra Ahuja, and Ming-Hsuan Yang. Deep laplacian pyramid networks for fast and accurate super-resolution. In *CVPR*, pages 624–632, 2017. 2, 1
- [19] Jaewon Lee and Kyong Hwan Jin. Local texture estimator for implicit representation function. In *CVPR*, pages 1929–1938, 2022. 2, 4, 5, 3
- [20] Ao Li, Le Zhang, Yun Liu, and Ce Zhu. Feature modulation transformer: Cross-refinement of global representation via high-frequency prior for image super-resolution. In *ICCV*, pages 12514–12524, 2023. 2
- [21] Jingyun Liang, Jiezhong Cao, Guolei Sun, Kai Zhang, Luc Van Gool, and Radu Timofte. Swinir: Image restoration using swin transformer. In *CVPRW*, pages 1833–1844, 2021. 1, 2, 3
- [22] Bee Lim, Sanghyun Son, Heewon Kim, Seungjun Nah, and Kyoung Mu Lee. Enhanced deep residual networks for single image super-resolution. In *CVPRW*, pages 136–144, 2017. 2, 3, 5, 7, 1
- [23] Wenzhe Liu, Hao Lu, Hongtao Fu, and Zhiguo Cao. Learning to upsample by learning to sample. In *ICCV*, pages 6027–6037, 2023. 5
- [24] Yong Liu, Hang Dong, Boyang Liang, Songwei Liu, Qingji Dong, Kai Chen, Fangmin Chen, Lean Fu, and Fei Wang. Unfolding once is enough: A deployment-friendly transformer unit for super-resolution. In *ACMMM*, pages 7952–7960, 2023. 2
- [25] David Martin, Charless Fowlkes, Doron Tal, and Jitendra Malik. A database of human segmented natural images and its application to evaluating segmentation algorithms and measuring ecological statistics. In *ICCV*, pages 416–423. IEEE, 2001. 7
- [26] Yusuke Matsui, Kota Ito, Yuji Aramaki, Azuma Fujimoto, Toru Ogawa, Toshihiko Yamasaki, and Kiyoharu Aizawa. Sketch-based manga retrieval using manga109 dataset. *Multimedia tools and applications*, 76:21811–21838, 2017. 7
- [27] Ben Mildenhall, Pratul P. Srinivasan, Matthew Tancik, Jonathan T. Barron, Ravi Ramamoorthi, and Ren Ng. Nerf: Representing scenes as neural radiance fields for view synthesis. In *ECCV*, 2020. 2
- [28] Abhisek Ray, Gaurav Kumar, and Maheshkumar H Kolekar. Cfat: Unleashing triangular windows for image super-resolution. In *CVPR*, pages 26120–26129, 2024. 2
- [29] Wenzhe Shi, Jose Caballero, Ferenc Huszar, Johannes Totz, Andrew P Aitken, Rob Bishop, Daniel Rueckert, and Zehan Wang. Real-time single image and video super-resolution using an efficient sub-pixel convolutional neural network. In *CVPR*, pages 1874–1883, 2016. 2
- [30] Gaochao Song, Qian Sun, Luo Zhang, Ran Su, Jianfeng Shi, and Ying He. Ope-sr: Orthogonal position encoding for de-

- signing a parameter-free upsampling module in arbitrary-scale image super-resolution. In *CVPR*, pages 10009–10020, 2023. [2](#), [3](#), [4](#)
- [31] Long Sun, Jinshan Pan, and Jinhui Tang. Shufflemixer: An efficient convnet for image super-resolution. *NeurIPS*, 35: 17314–17326, 2022. [4](#)
- [32] Radu Timofte, Eirikur Agustsson, Luc Van Gool, Ming-Hsuan Yang, and Lei Zhang. Ntire 2017 challenge on single image super-resolution: Methods and results. In *CVPRW*, pages 114–125, 2017. [7](#)
- [33] Zhengzhong Tu, Hossein Talebi, Han Zhang, Feng Yang, Peyman Milanfar, Alan Bovik, and Yinxiao Li. Maxim: Multi-axis mlp for image processing. In *CVPR*, pages 5769–5780, 2022. [4](#)
- [34] Cristina N Vasconcelos, Cengiz Oztireli, Mark Matthews, Milad Hashemi, Kevin Swersky, and Andrea Tagliasacchi. Cuf: Continuous upsampling filters. In *CVPR*, pages 9999–10008, 2023. [2](#), [1](#), [3](#)
- [35] Ashish Vaswani, Noam Shazeer, Niki Parmar, Jakob Uszkoreit, Llion Jones, Aidan N Gomez, Łukasz Kaiser, and Illia Polosukhin. Attention is all you need. *NeurIPS*, 30, 2017. [2](#)
- [36] Xiaohang Wang, Xuanhong Chen, Bingbing Ni, Hang Wang, Zhengyan Tong, and Yutian Liu. Deep arbitrary-scale image super-resolution via scale-equivariance pursuit. In *CVPR*, pages 1786–1795, 2023. [2](#)
- [37] Syed Waqas Zamir, Aditya Arora, Salman Khan, Munawar Hayat, Fahad Shahbaz Khan, and Ming-Hsuan Yang. Restormer: Efficient transformer for high-resolution image restoration. In *CVPR*, pages 5728–5739, 2022. [2](#)
- [38] Roman Zeyde, Michael Elad, and Matan Protter. On single image scale-up using sparse-representations. In *Curves and Surfaces: 7th International Conference, Avignon, France, June 24-30, 2010, Revised Selected Papers 7*, pages 711–730. Springer, 2012. [7](#)
- [39] Leheng Zhang, Yawei Li, Xingyu Zhou, Xiaorui Zhao, and Shuhang Gu. Transcending the limit of local window: Advanced super-resolution transformer with adaptive token dictionary. In *CVPR*, pages 2856–2865, 2024. [2](#), [3](#), [5](#), [7](#), [1](#)
- [40] Xindong Zhang, Hui Zeng, Shi Guo, and Lei Zhang. Efficient long-range attention network for image super-resolution. In *ECCV*, pages 649–667. Springer, 2022. [2](#)
- [41] Xiang Zhang, Yulun Zhang, and Fisher Yu. Hit-sr: Hierarchical transformer for efficient image super-resolution. In *ECCV*, 2024. [2](#), [3](#), [5](#), [7](#), [1](#)
- [42] Yulun Zhang, Kunpeng Li, Kai Li, Lichen Wang, Bineng Zhong, and Yun Fu. Image super-resolution using very deep residual channel attention networks. In *ECCV*, pages 286–301, 2018. [2](#), [1](#)
- [43] Yulun Zhang, Yapeng Tian, Yu Kong, Bineng Zhong, and Yun Fu. Residual dense network for image super-resolution. In *CVPR*, pages 2472–2481, 2018. [2](#), [3](#), [4](#)
- [44] Mingjun Zheng, Long Sun, Jiangxin Dong, and Jinshan Pan. Smfanet: A lightweight self-modulation feature aggregation network for efficient image super-resolution. In *ECCV*, 2024. [2](#), [3](#), [6](#), [7](#), [1](#)
- [45] Yupeng Zhou, Zhen Li, Chun-Le Guo, Song Bai, Ming-Ming Cheng, and Qibin Hou. Srformer: Permuted self-attention for single image super-resolution. In *ICCV*, pages 12780–12791, 2023. [2](#), [3](#), [5](#), [6](#), [7](#), [1](#)

# Implicit Grid Convolution for Multi-Scale Image Super-Resolution

## Supplementary Material

The supplementary includes reasons not considering pre-upsampling architecture, detailed comparisons with similar methods, training details, ablation studies, experiments beyond the  $\times 4$  scale, additional visualizations of inter-scale correlations, quantitative and qualitative results compared to Arbitrary-Scale Super-Resolution (ASSR) methods, and finally, visual results on Out-Of-Distribution (OOD) scales.

### 6. Pre-Upsampling Architecture

Recently, most methods employing neural networks have adopted a post-upsampling architecture that extracts low-resolution (LR) features using an encoder and upsamples them in the final step to achieve super-resolution (SR). However, some early studies [9, 16] employed a pre-upsampling architecture, where LR images are upsampled using bicubic interpolation, followed by post-processing through a neural network to achieve SR. Pre-upsampling architecture can easily predict any arbitrary scale, but it requires tremendous computations since all operations are performed in high-resolution (HR) space. For this reason, recent studies targeting only SR do not consider pre-upsampling architecture, and we have also not mentioned it in the main manuscript.

### 7. Comparisons on LapSRN and MDSR

Before our research, attempts were made to train multiple scales simultaneously employing a single model. For example, LapSRN [18] aimed to stably train and predict  $\times 8$  scale by progressively upsampling the LR image. MDSR [22] extracts features from images and converts them to RGB images using scale-specific heads and tails while sharing a single feature extractor across all scales ( $\times 2$ ,  $\times 3$ , and  $\times 4$ ) to refine features from multiple scales. Our approach offers several advantages over LapSRN and MDSR. First, LapSRN requires computations in the HR space because of its progressive upsampling design, resulting in a significant computational burden. We demonstrate in Appendix 10 that our method can predict the  $\times 8$  scale without such excessive computational costs brought by progressive upscaling architecture. Additionally, MDSR independently trains each head and tail, which means heads and tails cannot learn multi-scale information, potentially negatively impacting performance.

### 8. Comparisons on CUF

The continuous upsampling filters (CUF) [34] is similar to our method in that it maps scale-equivariant conditions into convolution kernels using an INR-based hyper-network

and is converted efficiently when instantiated at the specific integer scales. However, our method offers some advantages in computational efficiency. To demonstrate our efficiency compared to CUF, we consider only the instantiated CUF, excluding the inefficiencies that arise from targeting Arbitrary-Scale Super-Resolution (ASSR). CUF performs scale-specific modulation using depth-wise convolution followed by depth-to-space ( $\mathcal{DS}$ ) to upsample, with two additional point-wise convolutions added to compensate for insufficient channel mixing. These additional point-wise convolutions in HR space result in significant computational overhead, similar to SPConv<sup>+</sup>. In Appendix 13, we demonstrate that instantiated IGConv<sup>+</sup> outperforms instantiated CUF in both efficiency and performance, highlighting the superiority of our approach that performs all heavy computation in LR space.

### 9. Training Details

This section describes the training details for each method. The training details are presented in Table 7. The training budget allocated to our framework matches that required by scale-specific methods for training at the  $\times 2$  scale. Consequently, our framework achieves a one-third reduction in the overall training budget (in terms of training time or GPU usage) compared to fixed-scale methods utilizing SPConv or SPConv<sup>+</sup>.

Table 7. Training details for each method.

Methods	PatchSize	BatchSize	Iteration	LR	EMA
EDSR [22]	48	16	300000	0.0001	✓
RCAN [42]	48	16	1000000	0.0001	✗
SMFANet+ [44]	64	64	1000000	0.001	✓
HiT-SRF [41]	64	64	500000	0.0005	✗
SRFormer [45]	64	32	500000	0.0002	✗
MambaIR-light [12]	64	32	500000	0.0002	✗
MambaIR [12]	64	32	500000	0.0002	✗

The training details of the methods adopting pre-training and fine-tuning strategies can be found in Table 8. ATD [39] adopted the pre-training strategy with a small patch size on the DF2K dataset, followed by fine-tuning with a larger patch size. In contrast, HAT [5] is pre-trained on the more extensive ImageNet dataset before being fine-tuned on the DF2K dataset.

Table 8. Training details for methods adopting the pre-training strategy.

Methods	(Phase) Dataset	PatchSize	BatchSize	Iteration	LR
ATD [39]	(1) DF2K	64	32	300K	0.0002
	(2) DF2K	96	32	250K	0.0002
HAT [5]	(1) ImageNet	64	32	800K	0.0002
	(2) DF2K	64	32	250K	0.00001

Table 9. Comparisons of fixed-scale upsamplers (SPConv<sup>+</sup>) and our proposed multi-scale upsamplers (IGConv<sup>+</sup>) on RCAN encoder at 4 scales ( $\times 2$ ,  $\times 3$ ,  $\times 4$ , and  $\times 8$ ). Results from SPConv<sup>+</sup>( $\times r$ ) are measured by each scale-specific model, while results from IGConv and IGConv<sup>+</sup> are measured by a **single model**.

Encoder	Scale	Upsampler	Set5	Set14	B100	Urban100	Manga109
RCAN [42]	2	SPConv <sup>+</sup> ( $\times 2$ )	38.27/0.9614	34.12/0.9216	32.41/0.9027	33.34/0.9384	39.44/0.9786
		IGConv <sup>+</sup>	38.23/0.9614	34.12/0.9217	32.38/0.9022	33.27/0.9383	39.39/0.9784
	3	SPConv <sup>+</sup> ( $\times 3$ )	34.74/0.9299	30.65/0.8482	29.32/0.8111	29.09/0.8702	34.44/0.9499
		IGConv <sup>+</sup>	34.86/0.9306	30.71/0.8490	29.34/0.8111	29.18/0.8712	34.66/0.9505
	4	SPConv <sup>+</sup> ( $\times 4$ )	32.63/0.9002	28.87/0.7889	27.77/0.7436	26.82/0.8087	31.22/0.9173
		IGConv <sup>+</sup>	32.68/0.9007	28.98/0.7907	27.83/0.7444	27.03/0.8118	31.60/0.9182
	8	SPConv <sup>+</sup> ( $\times 8$ )	27.31/0.7878	25.23/0.6511	24.98/0.6058	23.00/0.6452	25.24/0.8029
		IGConv <sup>+</sup>	27.34/0.7850	25.35/0.6513	25.04/0.6048	23.13/0.6454	25.45/0.8016

## 10. Beyond $\times 4$ Scale

Many recent SR studies have focused on three scales ( $\times 2$ ,  $\times 3$ , and  $\times 4$ ), and accordingly, we also trained and evaluated our framework on these three scales. However, some previous studies have evaluated four scales including  $\times 8$ . We wonder whether more challenging and complex scales can also be trained simultaneously. For this reason, we use RCAN [42] as the encoder to train and evaluate our model on four scales simultaneously including  $\times 8$ . As shown in Table 9, IGConv<sup>+</sup> achieves 0.13 dB improvements on PSNR on Urban100 $\times 8$  compared to SPConv<sup>+</sup>( $\times 8$ ). Note that IGConv<sup>+</sup> is trained for four scales simultaneously, compared to existing RCAN with SPConv<sup>+</sup>. This surprising result underscores our claim that a fixed-scale training approach is unnecessary and shows that learning higher scales is possible without a progressive upsampling architecture.

## 11. Ablation Study

To validate that every proposed method contributes to performance improvement, we conduct an ablation study by adding our proposal to RDN [43]. Table 10 demonstrates the performance improvement by replacing the upsampler with IGConv and adding frequency loss, IGSample, and FGRep. This indicates that our proposed methods effectively contribute to performance improvement.

Table 10. Ablation study on our proposed methods. FFT, IGS, and FGR denote frequency loss, IGSample, and FGRep, respectively.

Upsampler	FFT	IGS	FGR	Urban100 (PSNR)		
				$\times 2$	$\times 3$	$\times 4$
SPConv <sup>+</sup>				32.89	28.80	26.61
IGConv				33.06	28.97	26.82
IGConv <sup>+</sup>	✓			33.10	29.02	26.88
	✓	✓		33.15	29.08	26.95
	✓	✓	✓	33.17	29.12	26.96

## 12. More Visualizations on Inter-Scale Corr.

This section includes additional visualizations of convolution filters trained for capturing inter-scale correlations. As shown in Figure 7, all convolution filters from  $\mathcal{H}$  of RDN-IGConv<sup>+</sup> change continuously with variations in scale, demonstrating that  $\mathcal{H}$  effectively captures the inter-scale correlation.

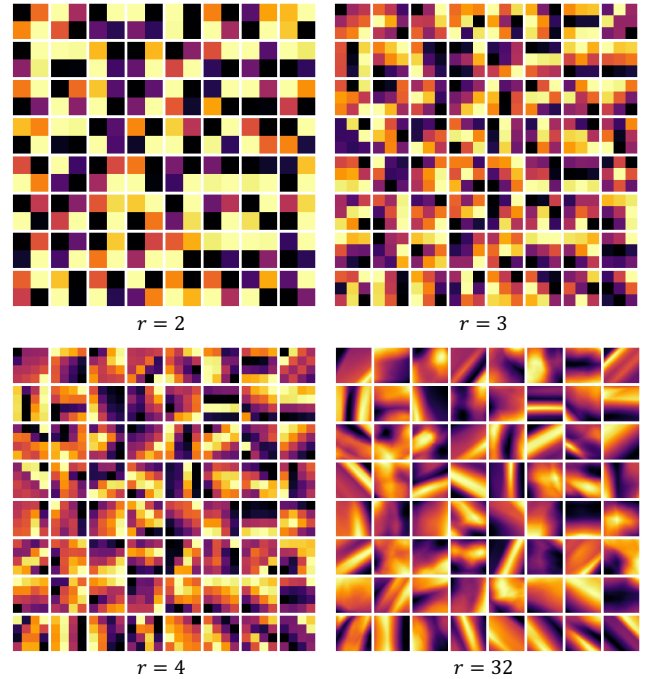


Figure 7. Visualizations of convolution filters inferred by  $\mathcal{H}$  of RDN-IGConv<sup>+</sup> for scales  $\times 2$ ,  $\times 3$ ,  $\times 4$ , and  $\times 32$ .

## 13. Comparisons on Arbitrary-Scale Methods

We also compare our method to ASSR methods since they share similar architecture (a pair of a single encoder and single upsampler). For the comparison, we train



Table 11. Comparison of ASSR upsamplers with our proposal. Efficiency measures are calculated by upsampling a  $128 \times 128$  image using an A6000 GPU for  $\times 4$  scale. The best and second-best results are highlighted in bold and underlined, respectively. <sup>§</sup> denotes each method is instantiated to the  $\times 4$  scale.

Encoder	Upsampler	Latency (ms)	#Params (K)	Memory (mb)	Set5			Set14			B100			Urban100		
					$\times 2$	$\times 3$	$\times 4$	$\times 2$	$\times 3$	$\times 4$	$\times 2$	$\times 3$	$\times 4$	$\times 2$	$\times 3$	$\times 4$
RDN [43]	LIIF [6]	139.6	347	1811	38.17	34.68	32.50	33.97	30.53	28.80	32.32	29.26	27.74	32.87	28.82	26.68
	LTE [19]	166.0	494	1608	38.23	34.72	32.61	34.09	30.58	28.88	32.36	29.30	27.77	33.04	28.97	26.81
	CiaoSR [3]	395.5	1429	12378	<b>38.29</b>	<b>34.85</b>	<b>32.66</b>	<b>34.22</b>	<u>30.65</u>	<b>28.93</b>	<b>32.41</b>	<b>29.34</b>	<b>27.83</b>	<b>33.30</b>	<b>29.17</b>	<b>27.11</b>
	LM-LTE [13]	31.2	271	367	38.23	<u>34.76</u>	32.53	<u>34.11</u>	30.56	28.86	32.37	29.31	27.78	33.03	28.96	26.80
	OPE-SR [30]	15.6	<b>0</b>	339	37.60	<u>34.59</u>	32.47	33.39	30.49	28.80	32.05	29.19	27.72	31.78	28.63	26.53
	CUF [34]	- / 1.2 <sup>§</sup>	10	- / 132 <sup>§</sup>	38.23	34.72	32.54	33.99	30.58	28.86	32.35	29.29	27.76	33.01	28.91	26.75
	<b>IGConv<sup>+</sup> (Ours)</b>	<b>2.3 / 0.5<sup>§</sup></b>	922	<b>71 / 43<sup>§</sup></b>	<u>38.26</u>	34.74	<u>32.64</u>	34.10	<b>30.68</b>	<u>28.91</u>	<u>32.39</u>	<u>29.33</u>	<u>27.82</u>	<u>33.17</u>	<u>29.11</u>	<u>26.96</u>
SwinIR [21]	LIIF [6]	342.8	614	5015	38.28	34.87	32.73	34.14	30.75	28.98	32.39	29.34	27.84	33.36	29.33	27.15
	LTE [19]	166.0	1028	1619	38.33	<u>34.89</u>	<u>32.81</u>	34.25	30.80	29.06	32.44	29.39	27.86	33.50	29.41	27.24
	CiaoSR [3]	889.9	3168	34760	<b>38.38</b>	<b>34.91</b>	<b>32.84</b>	<b>34.33</b>	<u>30.82</u>	<u>29.08</u>	<b>32.47</b>	<b>29.42</b>	<u>27.90</u>	<b>33.65</b>	<u>29.52</u>	<b>27.42</b>
	LM-LTE [13]	31.4	538	376	38.32	34.88	32.77	34.28	30.79	29.01	<u>32.46</u>	29.39	27.87	33.52	29.44	27.24
	CUF [34]	- / 3.6 <sup>§</sup>	<b>37</b>	- / 376 <sup>§</sup>	38.34	34.88	32.80	<u>34.29</u>	30.79	29.02	32.45	29.38	27.85	33.54	29.45	27.24
	<b>IGConv<sup>+</sup> (Ours)</b>	<b>4.6 / 0.8<sup>§</sup></b>	1991	<b>215 / 52<sup>§</sup></b>	<u>38.35</u>	<u>34.89</u>	32.79	34.18	<b>30.84</b>	<b>29.09</b>	<u>32.46</u>	<u>29.41</u>	<b>27.91</b>	<u>33.60</u>	<b>29.53</b>	<u>27.35</u>

Table 12. Comparison of ASSR upsamplers with our proposal trained for arbitrary-scale on non-integer scales. The best and second-best results are highlighted in bold and underlined, respectively.

Encoder	Upsampler	Set5			Set14			B100			Urban100		
		$\times 1.5$	$\times 2.5$	$\times 3.5$	$\times 1.5$	$\times 2.5$	$\times 3.5$	$\times 1.5$	$\times 2.5$	$\times 3.5$	$\times 1.5$	$\times 2.5$	$\times 3.5$
RDN [43]	LIIF [6]	41.43	36.15	33.56	37.45	31.87	29.56	35.83	30.48	28.42	<u>36.79</u>	30.49	27.64
	LTE [19]	<b>41.51</b>	<u>36.18</u>	<b>33.64</b>	<b>37.55</b>	<u>31.91</u>	<u>29.62</u>	<u>35.87</u>	<u>30.51</u>	<u>28.45</u>	<b>36.97</b>	<u>30.64</u>	<u>27.77</u>
	LM-LTE [13]	<u>41.49</u>	<u>36.18</u>	<u>33.62</u>	<u>37.52</u>	<u>31.91</u>	29.58	<b>35.88</b>	<b>30.52</b>	<u>28.45</u>	<b>36.97</b>	30.62	<u>27.77</u>
	OPE-SR [30]	40.24	35.85	33.49	36.02	31.67	29.55	35.07	30.33	28.38	33.47	30.08	27.48
	<b>IGConv<sup>+</sup><sub>arb</sub></b>	41.25	<b>36.20</b>	<b>33.64</b>	37.40	<b>32.00</b>	<b>29.68</b>	35.74	<u>30.51</u>	<b>28.46</b>	36.64	<b>30.70</b>	<b>27.85</b>

and evaluate our upsampler, IGConv<sup>+</sup>, using RDN [43] and SwinIR [21], which are commonly used as encoders in ASSR methods. The baselines for comparison include LIIF [6], LTE [19], CiaoSR [3], OPE-SR [30], CUF [34], and LM-LTE [13]. As shown in Table 12, SwinIR-IGConv<sup>+</sup> achieves a 0.01 dB higher PSNR on B100 $\times 4$  compared to SwinIR-CiaoSR while reducing latency and memory usage by 99.5% and 99.4%, respectively, demonstrating exceptional performance-efficiency trade-off. Moreover, instantiated IGConv<sup>+</sup> outperforms the instantiated CUF achieving a 0.06 dB higher PSNR on Urban100 $\times 2$ , with 78% and 86% lower latency and memory usage, respectively, suggesting that our efficiency is not merely due to the absence of non-integer scale prediction.

We also visually compare IGConv<sup>+</sup> with the ASSR methods (LIIF, LTE, and OPE-SR). In Figure 8, IGConv<sup>+</sup> demonstrates better visual quality and PSNR compared to the ASSR method. This confirms that IGConv<sup>+</sup> is efficient and has superior visual quality to the ASSR methods, highlighting the exceptional performance-efficiency trade-off of our method.

## 14. IGConv for Arbitrary-Scale

Since our method’s core operators are convolution and depth-to-space, it is only able to upsample an integer scale. While, by predicting  $\lceil r \in \mathbb{R} \rceil$  and then bicubic downsampling to  $r$ , our methods can predict any arbitrary scales

while this is not an optimal approach. To validate the performance of this simple implementation, we train and evaluate IGConv<sup>+</sup><sub>arb</sub>, which learns arbitrary float scales  $r \in [1, 4]$  using the aforementioned methods to learn arbitrary-scale and compare it with ASSR methods on non-integer scales. In this case, size factor  $s_r$  can be estimated by arbitrary float scale  $r$  while coordinates  $C_r$  are still estimated from  $\lceil r \rceil$ . As shown in Table 12, despite its naive implementation, IGConv<sup>+</sup><sub>arb</sub> achieves results comparable to other methods.

## 15. Visual Results on OOD Scale

Since our main goal is training multiple integer scales simultaneously, IGConv<sup>+</sup> fails to predict OOD scale ( $\times 24$ ) reliably. In the figure 9, IGConv<sup>+</sup> results in unpleasant artifacts in the areas where the color changes abruptly. However, note that our IGConv<sup>+</sup> successfully restores fine details such as thin lines, with significantly reduced inference latency about  $\times 25$  compared to LM-LTE [13]. Thus, addressing these limitations while maintaining computational efficiency and performance should be considered as a future research work.

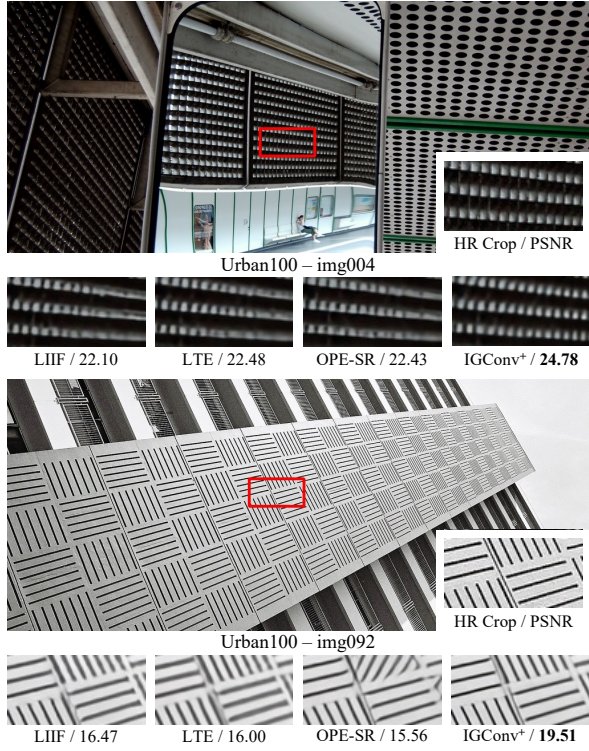


Figure 8. Visual comparisons on IGConv<sup>+</sup> and ASSR methods using RDN [43] encoder on Urban100 $\times$ 4 dataset. The best result on PSNR is bolded.

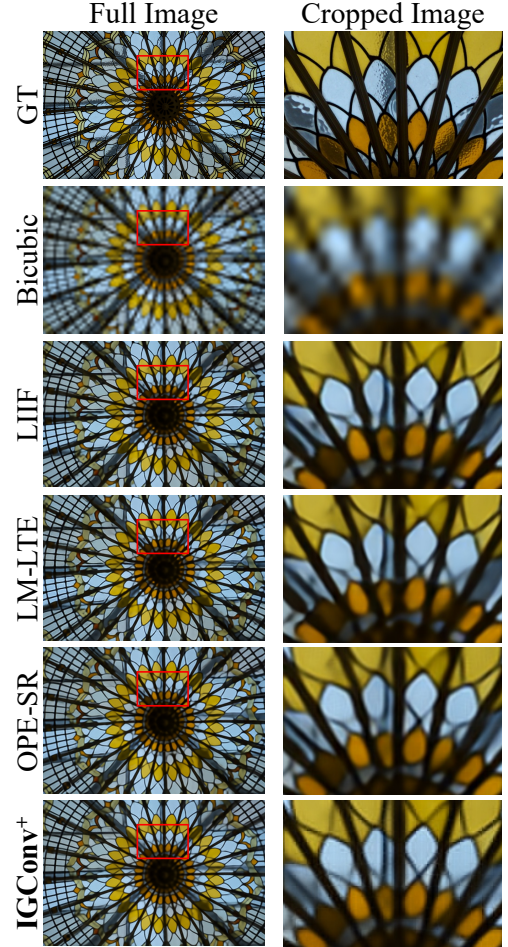


Figure 9. Visual comparisons on bicubic, ASSR methods [6, 13, 30], and our IGConv<sup>+</sup> using RDN [43] encoder on out-of-distribution scale ( $\times 24$ ). Cropped images correspond to the red bounding boxed area of full images.